CMOS-MEMS Membrane Gravimetric Biosensor

Anna Liao

CMU-RI-TR-06-10

August 2006

Robotics Institute
Carnegie Mellon University
Pittsburgh, Pennsylvania 15213

Abstract

A CMOS MEMS platform for gravimetric biosensing in liquid has been fabricated and tested. The concept is an aluminum and silicon dioxide membrane, coated with polystyrene and functionalized with receptors. When the protein analyte binds to the receptors, the sensor mass increases which causes a shift in the resonant frequency. The device is electrostatically actuated and the displacement is sensed with piezoresistors on the membrane edges. The MEMS membrane is expected to have a better mass sensitivity than previous millimeter scale devices (SAW, QCM, FPW), because it has a higher surface area to mass ratio. In addition, it can be actuated to oscillate at higher resonance modes and this may improve the quality factor in liquid. Initial experiments with a scanning laser Doppler vibrometer have resulted in the frequency response and modes of the membrane. This demonstrates the ability to actuate the membrane in higher modes and the corresponding resonant frequency values that should be detected through the piezoresistors. Future work includes verifying the optical results with electrical tests of the piezoresistors.

Contents

1 Introduction

Microelectromechanical systems (MEMS) are making an impact in information, automotive, and medical technologies. MEMS has the same advantages of miniaturization and integration that apply to microelectronics and are also including mechanical, acoustic, optical, magnetic, thermal, chemical, and biological components [1]. MEMS is already being used in CD/DVD laser heads, read-write heads for magnetic hard disks, frequency filters in cell phones, inertial sensors in the automotive industry, and micromirrors for digital display. Opportunities for MEMS in medical devices exist in biosensors, pacemakers, hearing aids, minimally invasive drug delivery, and retinal and neural implantable devices [2].

In this paper, the design and fabrication of the MEMS foundation for a biochemical gravimetric sensor is described, along with initial experimental results. The premise of this project is that a MEMS membrane provides a higher surface area to mass ratio for increased sensitivity compared to larger devices. The design incorporates the capability to actuate the higher modes of the membrane for possible improved performance in liquid, compared to previous resonant sensors. It should be noted that the sensor described in this report is not meant to be implantable, thus the issues regarding biocompatibility and *in vivo* sensing [2] are not discussed.

1.1 Biochemical Microsensors

Many biochemical sensor applications are focused on analyzing metabolites (e.g. adenosine triphosphate, oxygen, carbon dioxide, pH, glucose) at the single-cell level and making such sensor technologies implantable or noninvasive. There is also an interest in integrating sensors and testbench together in an efficient, high-throughput, multisample lab-on-a-chip system. A key feature of using MEMS for biosensing is that feature sizes approach the size of biomolecules, allowing for better analyte sensitivity. Microfabrication techniques allow for feature sizes ranging from millimeters to submicron. Microfluidics also plays an important part in nourishment, waste removal, or routing samples through the system.

The primary method for identification and quantification of biochemical substances is optically with fluorescent dyes and particles [3–6]. Optically-based sensors have the best sensitivity currently, but require large external optical equipment. Electrochemical sensors take advantage of electron transfer between an electrode and a redox reaction. [7–9]. Chemical field-effect transistor (FET) sensors are manufactured with established CMOS technology. Exposure to the target chemical results in a surface charge change at the interface between the insulator layer and overlying layer, and this is quantified by the change in the threshold voltage [7, 10]. Resonant sensors depend on target molecules absorbed in the sensing material to change certain properties that would be reflected in the resonant frequency [11–13]. Impedance sensors depend on target molecules absorbed in the sensing material to change the resistance [14]. Self-assembled monolayers have potential for better adherence of sensing material to the transducers [15, 16].

There are resonant devices in which the side dimension is greater than one millimeter and those with side dimension less than one millimeter. The former is referred to as small-scale devices and the latter is referred to as micro-scale devices. The prevalent small-scale resonators include quartz crystal microbalances (QCM), surface acoustic wave (SAW) devices, and flexural plate wave (FPW) devices. CMOS technology can be used to fabricate micro-scale resonators, such as cantilevers or membranes. Another promising micro-scale resonant sensor in liquid is the film bulk acoustic resonator (FBAR). Resonant devices have been used for measuring density and viscosity of liquids [17, 18], determining the rheological properties of polymer films [19], detecting organic vapors, and detecting biochemical active compounds by employing antibody-antigen, enzyme-substrate, and other receptor-protein pairs [20].

The earliest and best-known acoustic-wave sensor is the QCM, which is a piezoelectric AT-cut quartz crystal. When an AC voltage is applied across the electrodes located at the top and bottom of the crystal, the crystal oscillates at its resonant frequency. A QCM operating in liquid would have a shear movement relative to the fluid which is advantageous in that no normal components of the movement would result in acoustic energy loss to the liquid surroundings. The drawback is that the quartz crystal can only be lapped down to a certain thickness that is still much greater than those of the SAW, FPW, and membrane devices. This is the reason that the QCM has a low surface area to mass ratio, which results in low gravimetric sensitivity.

In SAW devices, the acoustic energy is concentrated within a region near the free surface of a single piezoelectric crystal whose thickness is a small fraction of a wavelength. The type of wave generated depends on the substrate material. These devices operate at hundreds of MHz and can attain gravimetric sensitivity an order of magnitude larger than a typical QCM device in air. The Rayleigh SAW device, made from ST-cut quartz, has wave displacement components normal to the liquid, which limits its usefulness in liquid. However, the surface transverse wave SAW device, usually made from lithium tantalate, has a contoured or coated free surface and an oriented crystalline structure that permits generation of a surface-bound acoustic wave with purely transverse particle motion. This drastically reduces acoustic energy loss to the environment.The acoustic plate mode (APM) sensor is either a thin plate of ST-quartz or $LiNbO_3$. Its wave displacement is completely shear relative to the liquid. The acoustic wave propagates on the top and bottom surface of the plate, providing for more energy transfer than the previous two SAW devices.

Flexural plate wave (FPW) devices consist of a piezoelectric film (silicon nitride or zinc oxide) located on one side of a thin supporting membrane, which is actuated via interdigitated conducting electrodes. Because of its location to one side of the neutral plane of the composite membrane, the deformation of the piezoelectric excites a propagating wave that involves flexure of the membrane. This anti-symmetric elastic wave has a low phase velocity relative to the surrounding liquid at low thicknesses. For this reason, there is little acoustic loss to the surrounding fluid. In addition, this device has a high surface are to mass ratio [20, 21].

Figure 1 shows the structures and properties of the described small-scale resonant devices.

There are generally two types of MEMS resonant devices, the cantilever and the membrane. Most biogravimetric cantilever devices have utilized static deflection, such that bending responses of cantilevers are associated with interaction between surface-immobilized receptors and the target analytes in solution. Deflection responses are

	QCM	Rayleigh SAW	SH SAW	SH APM	FPW
Substrate	AT-quartz	ST-quartz	$LiTaO_3$	$LiNbO_3$ ST-quartz	Si_xN_y/ZnO
Conceptual view		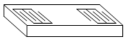	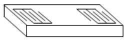	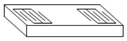	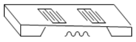
Wave mode	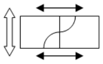	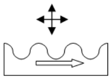	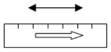	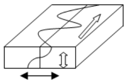	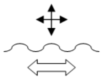
Medium	Gas Liquid	Gas	Gas Liquid	Gas Liquid	Gas Liquid

Figure 1: Structures and associated mode of operation for common small-scale acoustic resonators. Particle displacement is indicated by black arrows, while the direction of wave propagation is shown with an open arrow.

usually about 50 nm, but can reach microns with asymmetrical nanopatterning, and it can take from 5 to 60 minutes for the deflection to reach steady-state [22]. Cantilever devices in static mode tend to be long and compliant while those in resonant mode are short and stiff. The problems with static mode cantilever devices are the settling time and drift. Figure 2 is a diagram that shows the operation of a static mode cantilever.

The film bulk acoustic resonator (FBAR) consists of a piezoelectric material sandwiched between two electrodes. The first reported FBAR biochemical sensor in liquid uses a 10 x 10 x 1 μm^3 ZnO piezoelectric film and aluminum electrodes. [24] There is a silicon nitride supporting layer that is inert to most chemical solutions. The device is formed with a custom process that includes low pressure chemical vapor deposition (LPCVD), electron beam deposition, and sputtering the various layers together on a silicon wafer. The mode of propagation for the FBAR is bulk longitudinal waves along the film.

To the author's knowledge at the date of this writing, there are no other MEMS gravimetric resonant membrane devices for biomolecule detection in solution. MEMS resonant membrane devices operating in air have been used as tactile sensors, pressure sensors and acoustic microphones [25]. MEMS resonant membrane devices in liquid have been used as capacitive MEMS ultrasonic transducers (cMUTs) [26–28]. Resonant characteristics for devices operating in air seem to be well documented. Measurements of these devices in liquid have shown that they are inherently wideband, with frequency responses extending from 200 kHz to over 15 MHz, but it is difficult to make the devices perform predictably and repeatably [29]. A cMUT with an array of 30x30

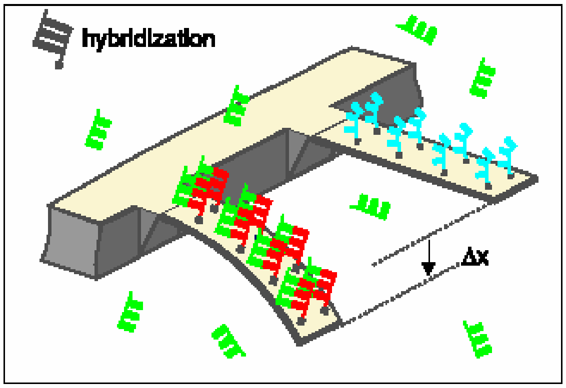

Figure 2: Diagram of a static mode cantilever DNA sensor. The surface of the cantilever is functionalized with receptors, and when the target analyte binds to the receptors, stress is induced in the cantilever causing it to bend [23].

polysilicon membranes of side lengths 20 to 100 μm and effective gap of 450 nm has the transient and frequency response in water shown in Figure 3 [28].

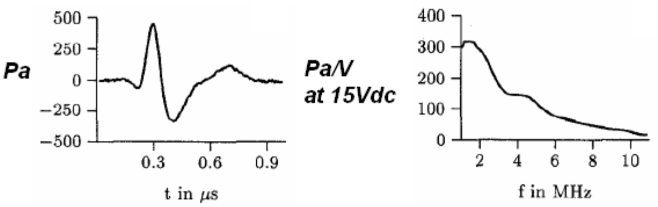

Figure 3: Transient and Frequency Response in water for a 30x30 array of polysilicon membranes of sidelengths 20 to 100 μm [28].

Some figures of merit for comparing gravimetric resonant sensors are quality factor Q, mass sensitivity S_m, and device sensitivity σ. Q defines the sharpness of the resonant peak, S_m specifies the fractional frequency change per mass per area loading, and σ specifies the mass change per frequency change. In Figure 3, the quality factor in water, approximated from the transient response, is $Q_{water} \approx 2$, while the quality factor in air, stated in the paper, is Q_{air} = 400. The quality factor of resonant devices are usually much higher in air than in liquid. Mass sensitivity S_m is given as [30]:

$$S_m = \lim_{\Delta m_a \to 0} \frac{(\Delta f)/f_0}{\Delta m_a} \tag{1}$$

where Δm_a is the added mass per unit area, Δf is the resonant frequency shift, and f_0 is the resonant frequency. Device sensitivity is given as:

$$\sigma = \frac{\Delta m_a a}{\Delta f} \tag{2}$$

where a is the surface area of the device and m is the mass of the device. The minimum detectable added mass per unit area depends on S_m and the noise in the resonator.

2 CMOS MEMS Gravimetric Sensors

Our device consists of a composite aluminum and silicon dioxide mesh membrane, clamped on all sides, in resonant mode operation. Figure 4 depicts the membrane. In the future, the membrane will be coated with a polymer which is a base for protein receptor immobilization chemistry. The membrane is actuated electrostatically by applying a sinusoidal voltage to the membrane with the silicon bulk as ground. The flexure of the oscillation is sensed with piezoresistors at the membrane edges. The chip, shown in Figure 5, consists of 16 membranes surrounded by bondpads. Two designs, grid (shown in Figure 6(a)) and brick (shown in Figure 6(b), have been fabricated to see which has better performance. The piezoresistors on each pair of horizontally adjacent membranes are connected in a Wheatstone bridge configuration particularly designed for either fundamental or second order mode operation.

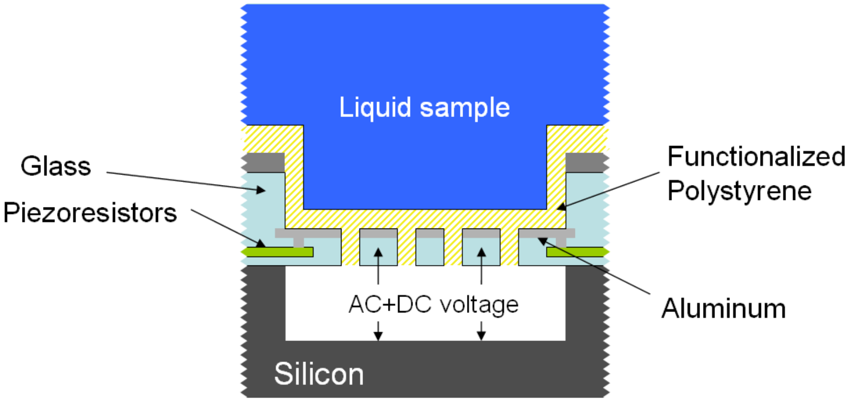

Figure 4: Side view diagram.

2.1 Resonant Sensing Principles

Gravimetric sensing is based on the fact that when the device mass increases, the resonant frequency of the device decreases. When mass attaches to the sensing surface, the frequency change of the resonant peak is detected. A higher quality factor allows for better resolution of detection.

The dynamic membrane in its fundamental modeis modeled as a classic mass-spring-damper system as shown in Figure 7. When an external force is applied to the system, the mass accelerates. However, the spring force, proportional to displacement, and the damping force, proportional to velocity, acts to oppose the external force. The

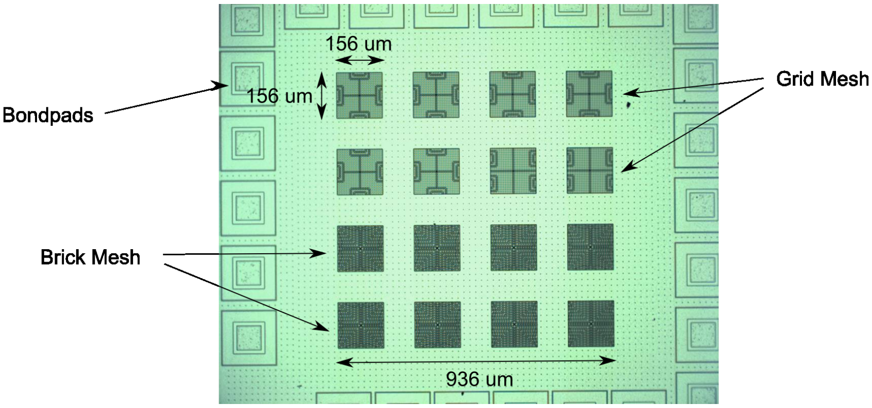

Figure 5: Optical microscope image of the entire chip.

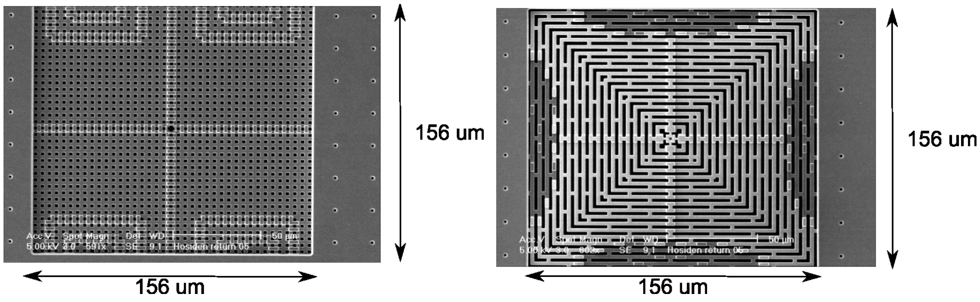

(a) Grid structure.

(b) Brick structure.

Figure 6: Scanning electron microscope (SEM) images of the membrane structures.

force equation is therefore:

$$F_{ext} = m\ddot{z} + b\dot{z} + kz \tag{3}$$

where F_{ext} is the external force, m is the effective mass of the resonating membrane, $\ddot{z}$ is the acceleration of the mass in the z-direction, b is the damping factor, $\dot{z}$ is the velocity of the mass in the z-direction, and k is the spring constant. The resonant frequency is defined as a function of k and m:

$$f_r = \frac{1}{2\pi}\sqrt{\frac{k}{m}} \tag{4}$$

The quality factor, or Q-factor, is the ratio of the energy stored in the system and the energy dissipated:

$$Q = 2\pi\frac{\text{maximum energy stored}}{\text{energy dissipated per cycle}} \tag{5}$$

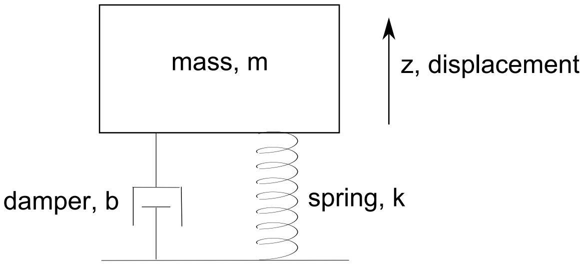

Figure 7: Mass-spring-damper system.

Systems with high Q-factor resonate with greater amplitude (at the resonant frequency) than systems with low Q-factor. Damping decreases the Q-factor. For $Q \gg 1$, the Q-factor can be defined as a function of the dynamic equation variables:

$$Q = \frac{\sqrt{mk}}{b} \tag{6}$$

The Q-factor can also be defined from the characteristics of the frequency response:

$$Q = \frac{f_r}{\Delta f_{3dB}} \tag{7}$$

where f_r is the resonant frequency and Δf_{3dB} is the bandwidth. Figure 8 shows the amplitude and phase transfer function for a resonant device. The bandwidth is the difference between the two frequencies where the amplitude drops 3 dB below the peak amplitude, A. There is also a phase change of -180^o at resonance.

Mass loading on the resonant structure decreases the resonant frequency of the system. The differential increase is derived from taking the derivative of f_r with respect to mass [31]:

$$\frac{df_r}{dm} = -\frac{1}{4\pi}\sqrt{\frac{k}{m^3}} \tag{8}$$

The frequency shift, Δf, for an applied mass change, Δm is:

$$\Delta f = -\frac{f_0}{4\pi m}\Delta m \tag{9}$$

where f_0 is the resonant frequency before mass loading and m is the mass of the membrane. The lower the mass of the resonant structure and higher the resonant frequency, the greater sensitivity of the sensor. This means that smaller and stiffer resonators will improve gravimetric sensitivity. Also, (9) can be substituted into (2) to obtain the equivalent form:

$$\sigma = \frac{4\pi m a}{f_0} \tag{10}$$

The ultimate minimum detectable frequency shift based on the thermal noise of the resonator [31, 32] is:

$$(\Delta f)_{min} = \frac{2}{X_0}\sqrt{\frac{f_0 k_B T f_{BW}}{kQ}} \tag{11}$$

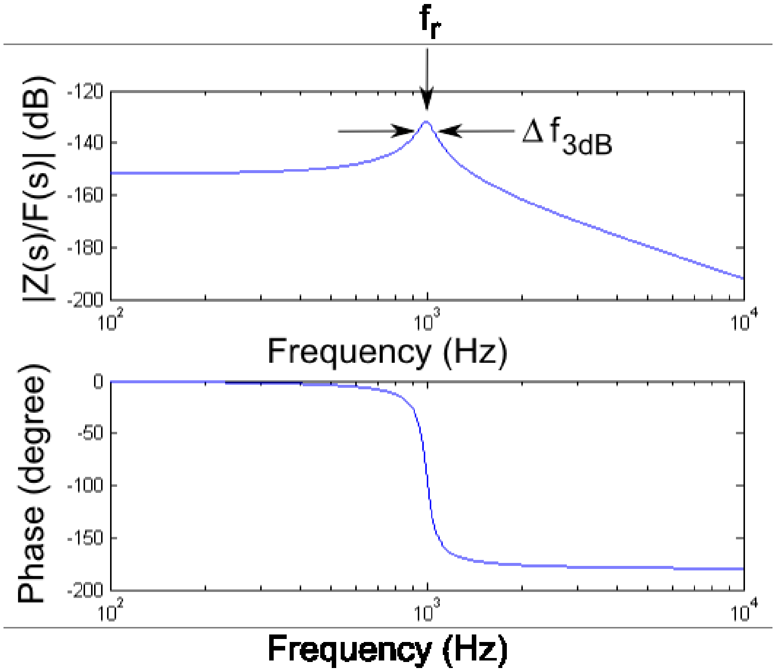

Figure 8: Amplitude and phase transfer function of resonant device with $m = 1$, $k = 3.95e7$, and Q = 10.

where X_0 is the oscillation amplitude, k_B is the Boltzmann's constant, T is the temperature, and f_{BW} is the frequency bandwidth. Combining (9) and (11) gives the minimum detectable mass:

$$(\Delta m)_{min} = \frac{8\pi m}{X_0}\sqrt{\frac{k_B T f_{BW}}{f_0 k Q}} \tag{12}$$

Other noise associated with the resonator and electronics will further increase this value.

After converting (8) to the form of (1), an alternate form of S_m is:

$$S_m = \lim_{\Delta m_a \to 0} \frac{(\Delta f/f_0)}{\Delta m/a} = -\frac{a}{4\pi m} \tag{13}$$

where Δm is the added mass, m is the mass of the resonator, and a is the surface area of the resonator. Increasing the surface area to mass ratio of the resonator should increase the mass sensitivity of the device. Table 1 summarizes surface area to mass ratio of various resonator devices and demonstrates why the membrane device should be advantageous compared to small-scale resonators.

Table 1: Surface area to mass ratio comparison for various gravimetric sensors [33].

Device	**Mass** (g)	**S.A.** (mm^2)	**Thickness** (μm)	**Operating Frequency** (Hz)	**S.A. to mass ratio** (cm^2/g)
SAW [34]	–	10	–	200 x 10^6	452
QCM [35]	0.14 g	154	300	5 x 10^6	11
FPW [36]	15 x 10^{-3}	600	25	2-30	400
MEMS membrane	94.4 x 10^{-9}	0.02	1.65	200 x 10^3	2120

2.2 Higher Mode Harmonic Resonance

For an FBAR device immersed in water, experimental results show that the quality factor for the second harmonic resonance is over three times better than the quality factor at the fundamental resonance [12]. It is hypothesized that there is less acoustic energy loss in the second harmonic resonance compared to the fundamental resonance, though it is uncertain why that is the case. Mass sensitivity remains about the same in air and in water, but reduced quality factor affects the minimum detectable signal adversely due to increased phase noise. In addition, it has been demonstrated on a QCM that measurement of the resonant frequencies at the fundamental mode and the third overtone can be used to distinguish between mass change effects and temperature change effects [37].

To investigate whether the higher modes of the membrane also improve the quality factor in liquid, our membrane device has been designed so that two additional higher modes can be actuated. The modes of the oscillating square membrane with fixed edges are defined as (m, n) where m and n are positive integers. (m, n) refers to the mode having a shape proportional to $\sin(mx)\cos(ny)$, where $x, y \in [0, \pi]$. The (1,1) mode is typically referred to as the fundamental mode. There is a different set of modes defined for the vibrations of a square membrane with free edges.

The membranes have electrical isolation joints that allow for an independent electrode for each quadrant, as shown in Figure 9. Details on the isolation joint design can be found in the Sensor Design section. These joints give us the ability to actuate the fundamental mode - (1,1) - and second order modes of the membrane - (1,2) and (2,2), shown in Figure 10. Experimental results in air have shown that the quality factor is improved for the higher modes, as summarized in table 2. In the future, we can perform experiments to see if higher order modes of the membrane will allow for an improved quality factor in liquid.

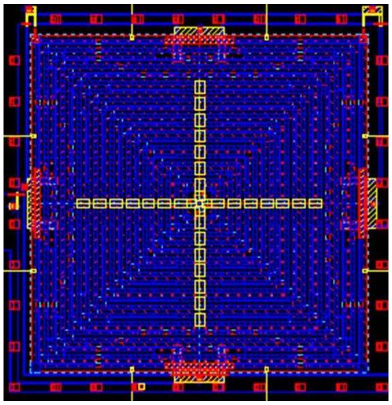

Figure 9: Cadence layout design for Isolation joints separate the independent electrode of each quadrant.

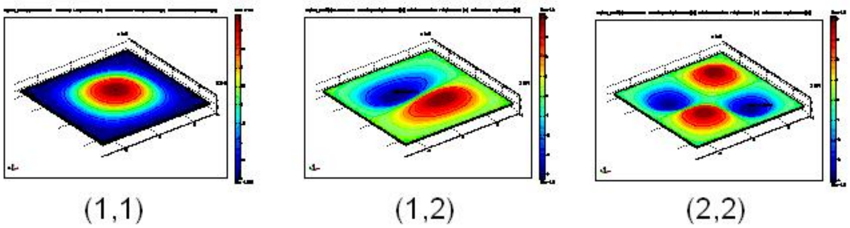

Figure 10: The membrane modes that can be actuated are (1,1), (1,2), and (2,2).

Table 2: Optical experimental results of quality factor measurement at modes (1,1), (1,2), and (2,2) [38]. The quality factor in air is improved for higher order modes of the membrane.

	(1,1)	**(1,2)**	**(2,2)**
Q_{air}	28	41	91

2.3 Electrostatic Actuation

The membrane is electrostatically actuated with a series-connected sinusoidal and DC voltage. When voltage is applied to two parallel-plate conductors, there is a force that pulls the two plates together. The sign convention for the electrostatic force is outwards, as shown in Figure 11.

The electrostatic force as a function of the applied voltage is:

$$F_e = \frac{1}{2}\frac{dC}{dz}V^2 \tag{14}$$

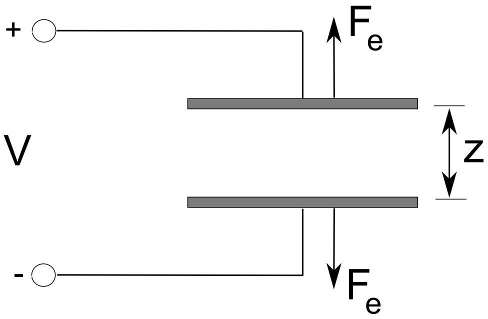

Figure 11: Electrostatic force acting on parallel-plate capacitor.

where $C = \frac{\epsilon_0 A}{g+z}$, A is the plate electrode area, g is the gap between the plates, and $V = V_{DC} + v_{ac}cos(\omega_{ac}t)$, such that V_{DC} is the input DC voltage, v_{ac} is the amplitude of the input AC voltage, and ω_{ac} is the frequency of input AC voltage. This results in the force expression:

$$F_e = -\frac{\epsilon_0 A}{2(g+z)^2}\left(\underbrace{V_{DC}^2 + \frac{v_{ac}^2}{2}}_{DC} + \underbrace{2V_{DC}v_{ac}cos(\omega_{ac}t)}_{\omega_{ac}} + \underbrace{\frac{v_{ac}^2}{2}cos(2\omega_{ac}t)}_{2\omega_{ac}}\right) \tag{15}$$

Note that the response has force components at three different frequencies: DC, input applied frequency, and twice the input applied frequency. Ignoring the DC component, the resulting z-displacement of the membrane is the sum of the cosine waves at the two frequencies, which is represented by the solid line in Figure12.

This concept can be used to measure the feedthrough in the system. When the input DC voltage is reduced to zero, the output response signal should have no ω_{ac} frequency component. If there is a ω_{ac} component in the response, it is either electrical feedthrough from the input signal or noise sources in the system.

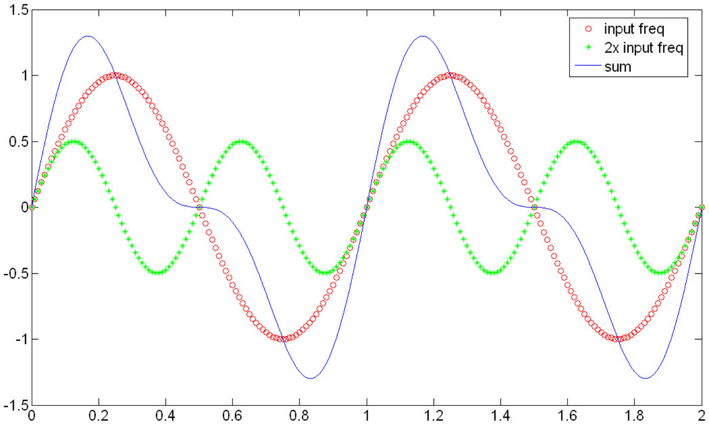

Figure 12: Sum of two sine waves (blue solid line), one at the input frequency (red circles) and the other at twice the input frequency (green asterisks).

2.4 Piezoresistive Sensing

Piezoresistivity is a material property where the bulk resistivity is related to the directional mechanical stresses applied to the material [39]. The mobility or the number of charge carriers in these materials change depending on the volume. Volume changes affect the energy gap between the valence and conduction bands. Highly piezoresistive materials, such as silicon, can be utilized for the transduction from mechanical to electrical domain.

Diffused polysilicon resistors are placed at the edges of the membrane to detect membrane deflection. The maximum stress is located at the center of the edge of the membrane [40]:

$$\sigma_{edge} = -\frac{Pw^2}{3.25h^2} \tag{16}$$

where P is the pressure applied to the membrane, w is the side length of the square membrane, and h is the membrane thickness.

Strain, σ_o, in the piezoresistors results in a change in resistance,ΔR:

$$\frac{\Delta R}{R} = (\pi_l + \nu\pi_t)\sigma_o \tag{17}$$

where R is the resistance when there is no strain, π_l is the longitudinal piezoresistive coefficient, and π_t is the transverse piezoresistive coefficient. The piezoresistors from two adjacent membranes are connected together in a Wheatstone bridge configuration, as shown in figure 13. The piezoresistors are connected such that the differential output from the bridge is maximized. There are four different configurations for each design (brick and grid), based on the different modal excitations, with each membrane pair as mirror images of each other.

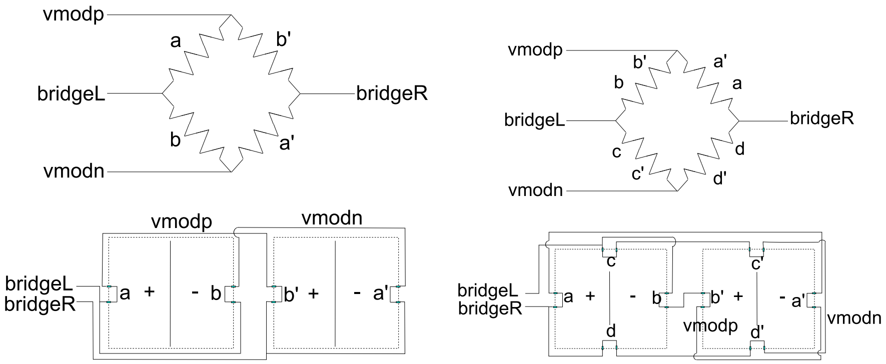

(a) (1,2) mode configuration.

(b) Another (1,2) mode configuration. Piezoresistors at top and bottom edge of membrane should have no change at (1,2) mode excitation, but it can be used as a redundancy check for correct mode or fabrication offsets.

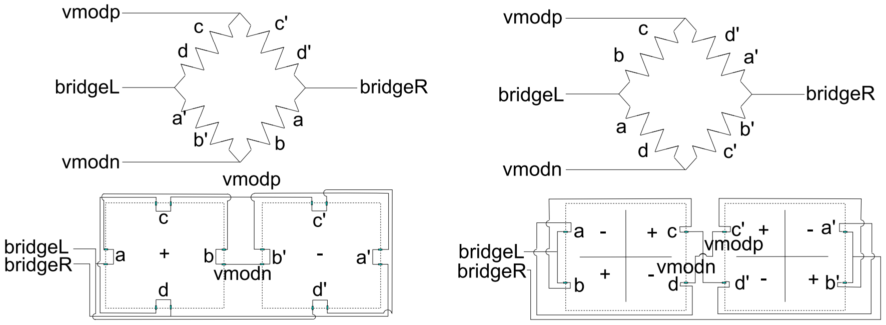

(c) Fundamental (1,1) mode configuration.

(d) (2,2) mode configuration.

Figure 13: Wheatstone bridge schematics with associated layout configurations for the different modes. Each piezoresistor block is approximately 500 Ω. Dashed line represents location of square membrane.

3 Immobilization Chemistry

Polystyrene is coated on the membrane to seal the electronics from the liquid and also to be functionalized with receptors. Polystyrene as a base for photochemistry has been well characterized in the literature [41, 42]. It dissolves easily in an organic solvent, such as toluene, and can be easily cast on to the mesh as a thin layer, either with spincoating or pipetting. It conforms nicely to the mesh and fills in the void areas well. Most importantly, it forms a rigid film and is tightly bound to the surface. Less energy is dissipated for a tightly bound layer compared to a viscoelastic coating.

3.1 Polystyrene Coating

Polystyrene can be coated on the membrane by spincoating. Figure 14 shows that this method provides a conformal polymer layer of approximately 1 μm. However, one problem is that the bondpads will also be coated. It would be difficult to dissolve the polymer from the bondpads since this will probably leave a residue. This may complicate wirebonding from the bondpads to the DIP package, since a clean surface on the bondpad is required. Another option is to use a type of polystyrene that can be patterned with photolithography to remove material over bondpads [43]. This method has not been investigated for our application, but may be considered in the future.

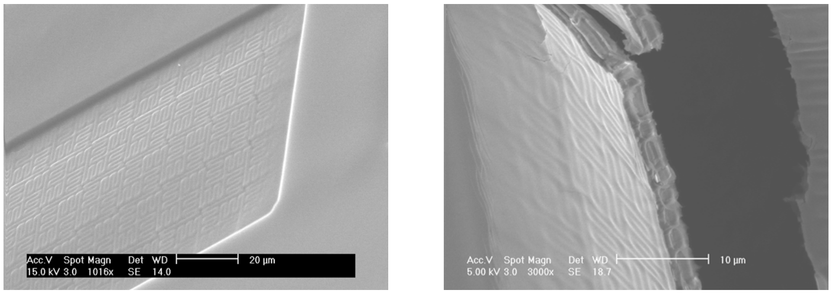

(a) Membrane surface after polymer coating.

(b) Torn membrane to show cross-section of polymer coating.

Figure 14: SEM images of polystyrene spincoated on the surface of a MEMS mesh membrane [33].

Polystyrene can also be jetted onto the surface of the membrane. This will allow polystyrene coating in selective areas without touching the bondpads. Figure 15 shows jetting of polystyrene on a 100 μm by 100 μm MEMS mesh structure [31]. This method does not seem to give a conformal coating as well as the spincoat method, due to the coffee ring effect [44], but may be the better option because of the bondpad problem.

3.2 Functionalized Surface

This biosensor uses a non-catalytic, affinity-based technique, which relies on the immobilization of a ligate to the surface. The ligand-ligate interaction can then be detected through gravimetric methods. The two most important challenges to overcome is the immobilization of the bioaffinity recognition element and prevention of non-specific interactions [33]. It is important to eliminate non-specific adsorption because this will also increase the mass of the device and result in increased error in the measurement.

The model ligand-ligate system we are using is the avidin-biotin system. One avidin molecule is capable of binding four biotin molecules specifically and very strongly. The dissociation equilibrium constant for the avidin-biotin binding interaction is on the order of 10^{-15} M. Table 3 compares different ligand-ligate systems, where MW is molecular weight, K_d is the dissociation constant, and B_O is number of binding sites.

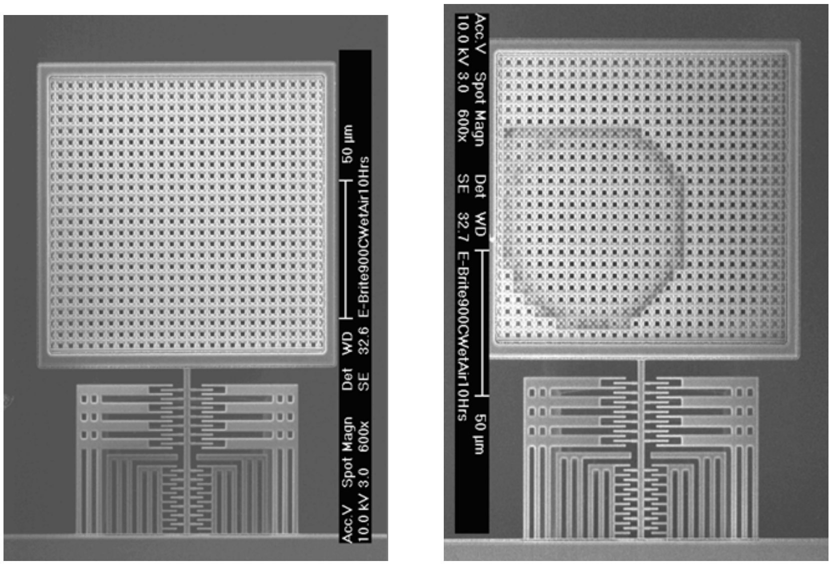

(a) No drops of polymer has been applied. Resonant frequency is 13.963 kHz.

(b) One drop of polymer has been applied. Resonant frequency is 13.927 kHz.

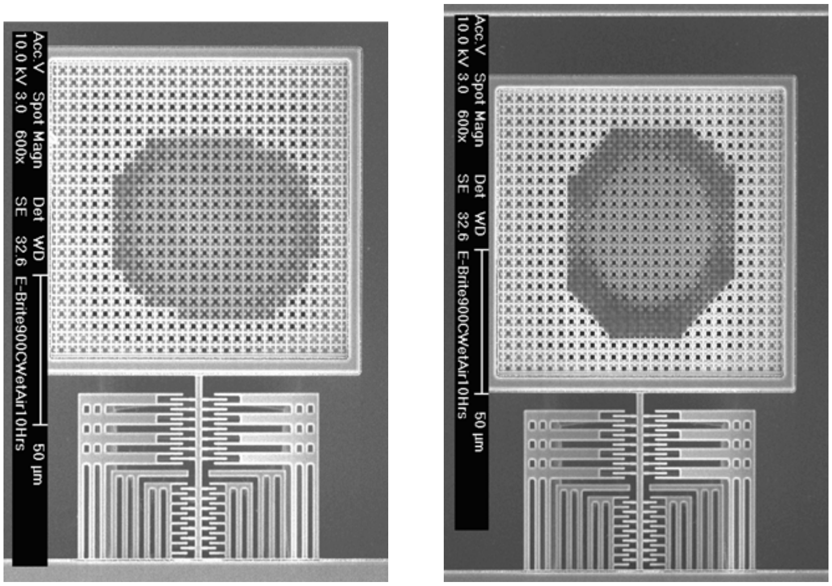

(c) Ten drops of polymer has been applied. Resonant frequency is 13.891 kHz.

(d) Twenty drops of polymer has been applied. Resonant frequency is 13.855 kHz.

Figure 15: SEM images of polystyrene jetted onto a 100 μm by 100 μm MEMS device [31].

Table 3: Ligand-ligate systems that can be applied to this sensor [33]

Application	**Target**	**MW (g/mol)**	**Immobilized Binding Group**	**MW (g/mol)**	**K_d (M)**	**B_O (mol/cm^2)**
Model System	Avidin	67000	Biotin	250	10^{-15}	9e-11
Model System	Biotin	250	Avidin	67000	10^{-15}	4e-12
Bioterrorism	anti-PA (IgG)	150000	Anthrax PA	82667	10^{-6}	1.3e-12
Cancer Detection	p53 Antigen	53000	anti-p53 anti-body (IgG)	150000	10^{-6}	1.1e-12

The procedure for functionalizing the surface is shown in Figure 16. Photobiotin (PHB) in solution is injected onto the surface. The PHB solution is lyophilized to remove the water, which means the surface is rapidly frozen and dehydrated under high vacuum. The surface is exposed to UV light for 10 minutes to immobilize the PHB. The surface can also be patterned through a UV mask, such that only specific areas will have PHB immobilized. This allows for mass loading on the anti-nodes (points of maximum motion) of the membrane, which increases device sensitivity [45] and can be used to detect multiple different analytes on a single membrane [46]. The surface is flushed with a pH 7 buffer to remove any PHB that has not been immobilized. Avidin in solution is then injected onto the surface and the surface is flushed with pH 7 buffer to remove any avidin that has not bound to the surface. Biotinylated protein, such as bovine serum albumin (BSA), can now be detected in solution. If CaptAvidin (a significantly more expensive form of avidin) is used, the binding of avidin to biotin can be reversed when pH 10 buffer is injected onto the surface. There can be many layers of this avidin-biotin sandwich assay, and it can be used for mass amplification if the attached mass is too low to be detected by the sensor.

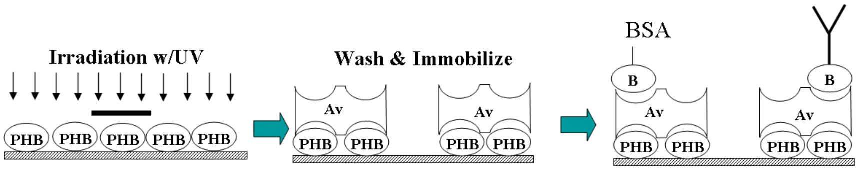

Figure 16: Immobilization of photobiotin to membrane surface and binding of target analytes [33].

4 Sensor Design

The sensors were designed within the constraints of the fabrication technology. This allows for the capability to manufacture multiple devices in a well established process. The computer-aided design (CAD) tool Cadence is used to generate the device layout. This software package also includes the capability for verification of the layout in comparison to the corresponding schematic and test simulation of circuit elements. From the optical measurements, membrane deflection amplitude is on the order of tens of picometers relative to a 10Vpp + 4 Vdc input signal. Printed circuit board (PCB) amplifiers were designed for the input and output signals. This was necessary to generate a larger deflection amplitude and to increase the output signal beyond the measurement system noise floor. A prototype of the packaging to incorporate the sensor and fluid channels has also been built.

4.1 CMOS MEMS micromachining

Our membrane structures were fabricated using a standard complementary metal-oxide-semiconductor (CMOS) process and released in the Carnegie Mellon University Nanofabrication Facility. While the materials available and layer thickness are restricted to the foundry processes, the advantages of using CMOS are cost, reliability, high yield, and integration of sensors and circuits. Chips were fabricated in the Jazz SiGe 0.35 μm 4-metal process [47].

The process flow for structural release is shown in Figure 17. The mesh structures were released from the silicon substrate in a two-step etch process. The first step consists of a 5 hour CHF_3/O_2 anisotropic reactive ion etch (RIE) of the overglass and dielectric layers, using the Plasma-Therm 790 RIE System located in the Carnegie Mellon Nanofabrication Facility. Next, the Surface Technology Systems (STS) deep silicon inductively coupled plasma (ICP) RIE system is used for a 3 minute SF_6/O_2 isotropic etch of the silicon bulk underneath the membrane. Upon release, the MEMS chips were then mounted to a dual in-line packages (DIPs) with silver epoxy (CW2400 from Circuitworks). The bondpads were then wire bonded to the DIP using a West-Bond semi-automatic wire bonder. The mounted chips were placed in a protoboard. The polystyrene polymer, used as a foundation for the functionalization chemistry, was deposited on the membrane with a custom inkjet system.

4.2 Layout Design

There are some design considerations when generating the layout for the device:

1. Drive signal feedthrough is minimized by placing a ground plane between actuation lines that crossover.

2. Minimum gaps are defined by the foundry and post-release process requirements.

3. Piezoresistors need to be shielded by metal to avoid being removed in the etch process, as shown in Figure 18.

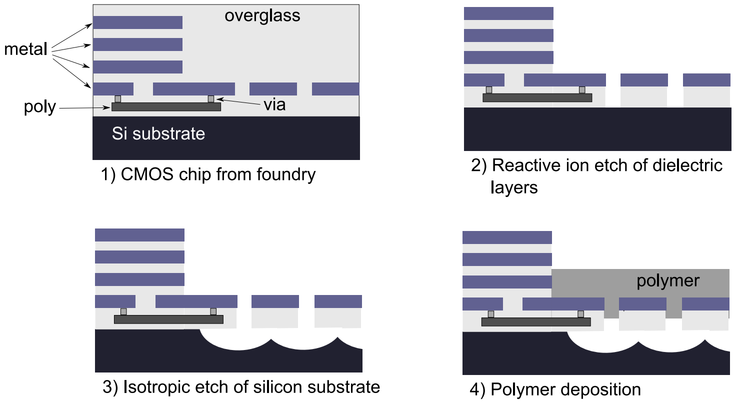

Figure 17: Process flow of structural release, viewed at cross-section of membrane edge where polysilicon resistor is located. The drawings are not to scale.

4. Residual stress and stress gradients in the aluminum and silicon dioxide cause bending, such that it is uncertain whether the membrane will bow upwards or downwards. This effect is minimized by eliminating the thermally grown field oxide layer in the design but it is impossible to remove all internal stresses.

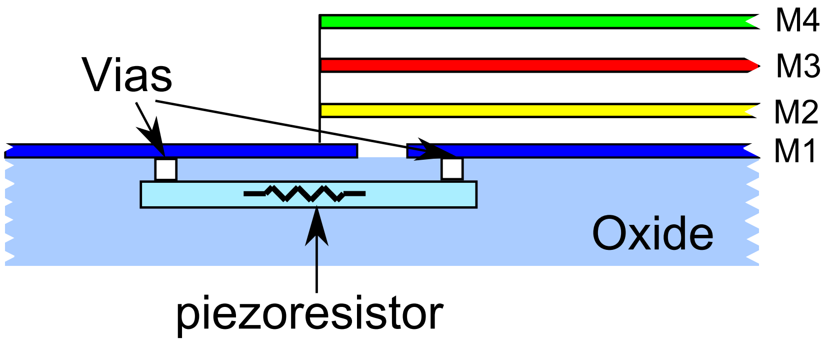

Figure 18: Metal shielding of piezoresistors at edge of membrane.

The grid structure, shown in Figure 6(a) has a structural mass of 80 ng and void space of 28%. The brick structure, shown in Figure 6(b) has a structural mass of 57 ng and void space of 50%. While the brick structure is more flexible and hopefully will allow greater amplitude of oscillation, there is less electrode area than the grid structure. There are isolation joints that separate the membrane into four quadrants. This allows the ability to actuate the second-order harmonic resonance modes. Isolation joints are also used to separate the membrane drive force from the piezoresistor signal pathway. A cross-section of an isolation joint is shown in Figure 19. The bottom metal and oxide represent the primary layers that compose the membrane. The top metal piece connects two adjacent quadrants through oxide pieces, so the two quadrants are electrically isolated.

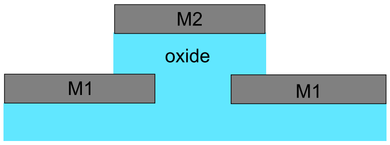

Figure 19: Isolation joint cross-section.

4.3 PCB amplifiers

Printed circuit board (PCB) amplifiers were designed and fabricated for the input and output signal, shown in Figure 21. The input signal was originally supplied by a waveform generator (limited to ±10 V) and amplified with a stereo amplifier (bandwidth at 100 kHz). The magnitude frequency response of the amplifier is shown in figure 20. Since the fundamental mode of the membrane is at 250 kHz, the gain of the amplifier at that frequency is only 9.85 dB. The input signal conditioning circuit (gain = 18.63 dB at 250 kHz) produces the non-inverted and inverted amplified versions of the source signal, Vin, with DC voltage bias, Vdc. The output signal conditioning circuit (gain = 25.44 dB at 250 kHz) is an instrumentation amplifier circuit.

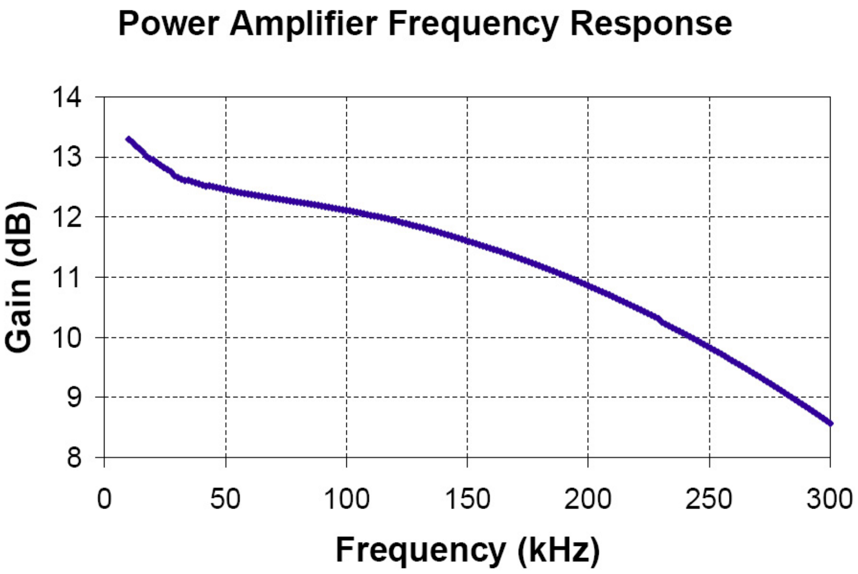

Figure 20: Network analyzer measurement of stereo amplifier gain spectrum. Note that the gain at 250 kHz is 9.85 dB.

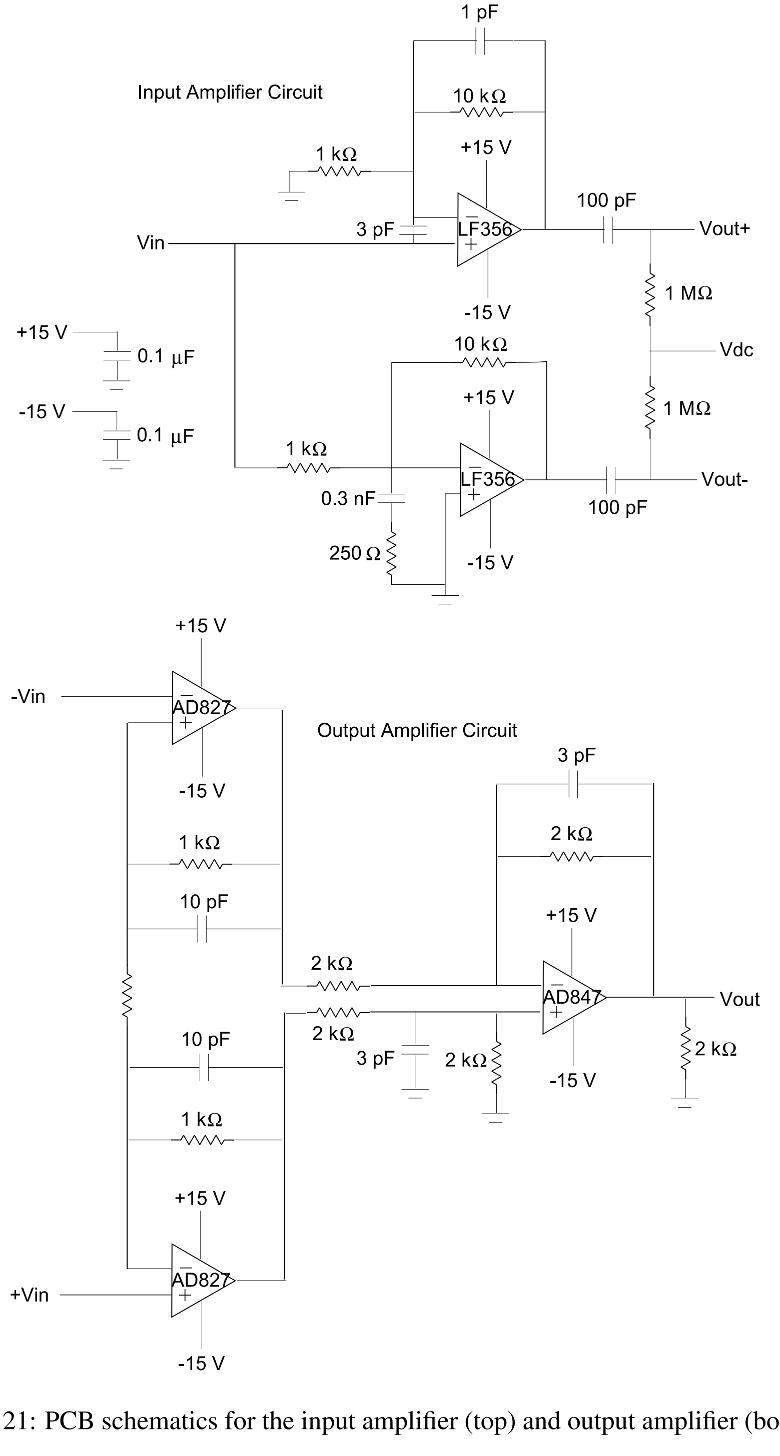

Figure 21: PCB schematics for the input amplifier (top) and output amplifier (bottom).

4.4 Packaging

An acrylic microfluidic clamshell reservoir, shown in Figure 22, was constructed for liquid sample introduction and removal, as well as isolation of the mechanical structures from the electronics [33]. The M-300 Laser platform from Universal Laser Systems, Inc. [48] was used to engrave features in the plastic, by melting and vaporizing the surface. Many plastics were tested, including acetal copolymer, polycarbonate, acrylonitril-butadiene-syrene (ABS), polypropylene, and glass. It was found that acrylic had the best results when processed with the laser system.

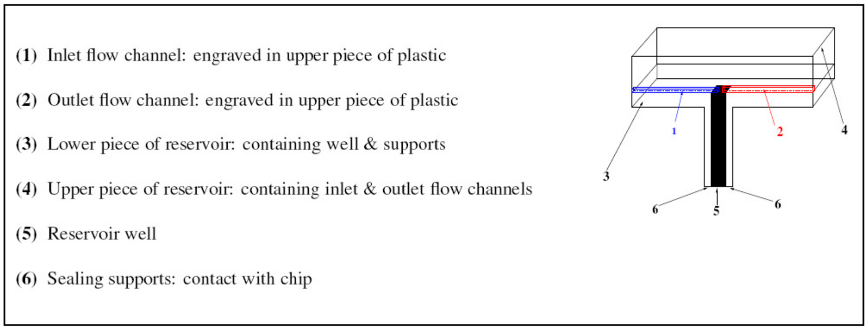

Figure 22: Cross-sectional diagram of acrylic clamshell reservoir [33]. Drawing is not to scale.

The reservoir is formed from two acrylic pieces fastened together with clamps and acrylate glue. The bottom piece contains a well that allows the liquid to come in contact with the membrane. The top piece contains the inlet and outlet flow channels to and from the reservoir. Injection of sample liquid is done by gluing a needle to the inlet and using a syringe. Figure 23 shows detailed photos of the plastic reservoir design. A dye solution was injected to test for leakage. To inhibit nonspecific adsorption to the exposed surfaces of the reservoir, it was soaked in bovine serum albumin (BSA) in phosphate-buffered saline (PBS) solution to passivate the surface [42].

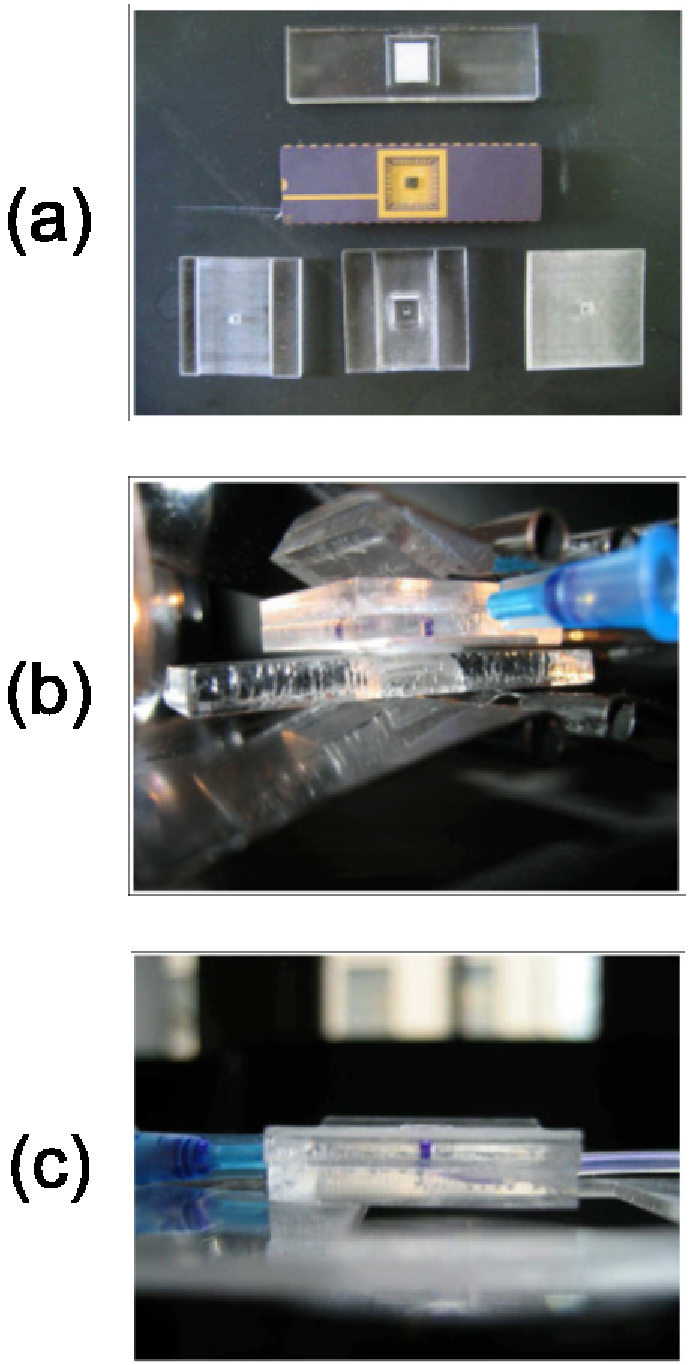

Figure 23: Reservoir design: (a) size comparison of packaging to wirebonded chip, (b) clamped reservoir with needle, and (c) leakage test with dye [33]

5 Sensor Experiments

5.1 Out-of-plane Displacement Measurements

The Polytec Laser Doppler Vibrometer (LDV) OFV-3001 is used to make non-contact velocity measurements on moving surfaces. These measurements can be integrated to obtain the displacements. Laser vibrometers are typically two-beam interferometer devices which detect the phase difference between an internal reference and the measurement beam. A differential measurement is taken with one laser head focused on the stationary surface of the package and another laser head focused on the membrane surface. This is to reduce the effect of the vibration noise in the chip package. Measurements can be taken with a waveform generator and oscilloscope, as shown in Figure 24(a), or with the Agilent 4395A Network Analyzer, as shown in Figure 24(b). The network analyzer sweeps through a large range of frequencies at small increments, but the output voltage is smaller than that of the waveform generator and it only measures the response at the frequency of the input signal. Taking measurements with the waveform generator and oscilloscope takes longer, because the frequency of the input signal is manually adjusted. The frequency responses of the brick and grid structures, including the effect from the limited bandwidth of the stereo amplifier are shown in Figure 25. There is no way to know for certain what mode the resonant peaks represent with the OFV-3001. We were able to verify the modes corresponding to the resonant frequencies when we acquired the improved LDV system, as described in the following experiments. The peaks at approximately 250 kHz and 350 kHz represent the fundamental mode resonant frequency for the brick and grid designs, respectively. The peak at approximately 850 kHz correspond to the (1,3) mode for the brick design.

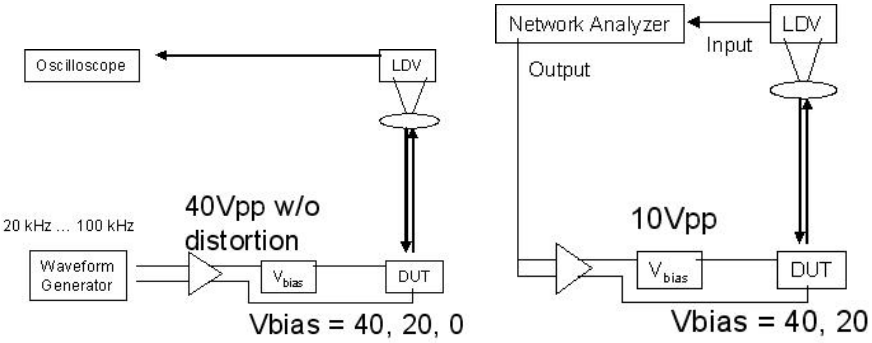

(a) With waveform generator and oscilloscope.

(b) With network analyzer.

Figure 24: Laser Doppler vibrometer experimental setups.

Videos of the three-dimensional dynamic mechanical response of the membrane were imaged with the Polytec Micro System Analyzer (MSA-400). The MSA incorporates laser Doppler vibrometry with stroboscopic video microscopy to identify the in-plane and out-of-plane resonance modes. It allows for picometer resolution on out-of-plane displacements.

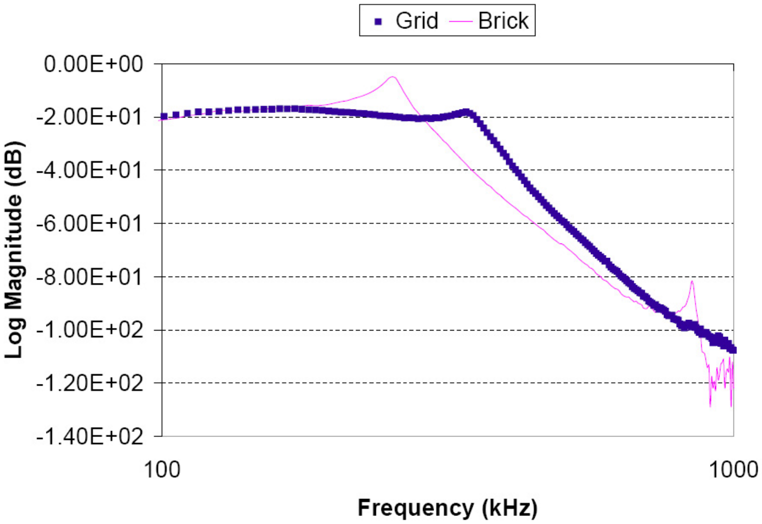

Figure 25: Frequency responses of the brick and grid structures.

A pseudo random signal is used to actuate the mesh. This type of input signal is used because it allows for faster measurement than a sine sweep and generally has higher signal-to-noise ratio with the assumption that the system is fairly linear. It is designed to excite all fast fourier transform (FFT) lines of the measured spectrum with the magnitude set for all frequencies to the same value. The phase is calculated as a uniformly distributed random number, giving the signal its random sound. Although the signal is called “pseudo random”, it is not a random signal. Once generated using random numbers for phase, it is repeated over and over again.

Both the fundamental (1,1) mode at 255 kHz and drum (1,3) mode at 845 kHz were identified when a uniform voltage (10Vpp+4Vdc) is applied to all quadrants of the membrane, as shown in Figure 26.

The (1,2) mode at 491 kHz, shown in Figure 27(a), is also present when the membrane is actuated such that the top two quadrants are actuated with a 8Vpp+4Vdc signal and the bottom two quadrants are actuated with an AC signal with the same DC-bias but 180 degree out-of-phase AC signal (-8Vpp+4Vdc). A similar electrode configuration is used to actuate the (2,2) mode at 931 kHz, in addition to the fundamental and drum modes.

The frequency response for each type of different actuation is summarized in Figure 28. Notice that the fundamental (1,1) and drum (1,3) modes appear for all actuation schemes, but the (1,2) and (2,2) modes only appear when the membrane is specifically actuated for that mode.

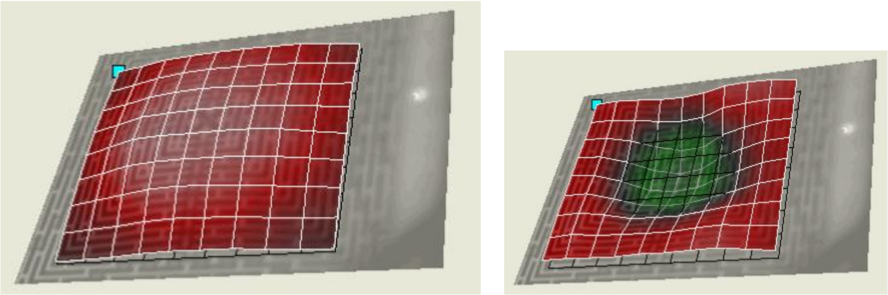

(a) Fundamental mode (1,1) at 255 kHz.

(b) Drum (1,3) mode at 845 kHz.

Figure 26: Modes of the membrane under 1 MHz visible when a uniform voltage is applied on the membrane.

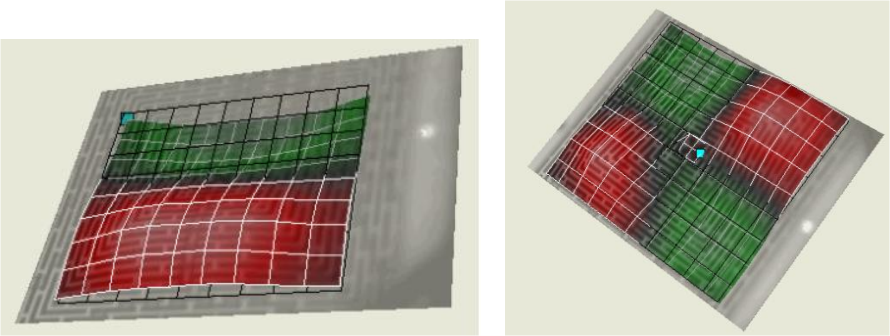

(a) (1,2) mode when the membrane is actuated such that the signal applied to the top two quadrants are 180 degrees out-of-phase from the signal applied to the bottom two electrodes.

(b) (2,2) mode present when the membrane is actuated in the (2,2) configuration.

Figure 27: Modes of the membrane under 1 MHz visible when a uniform voltage is applied on the membrane.

6 Future Work

The membrane modes have been measured optically, but it is imperative to be able to obtain the same spectrum using the piezoresistors on the edges of the membrane. Once it is confirmed that the piezoresistors are reliable for determining the displacement, the sensor is ready to be tested in liquid.

One of the main issues with the membrane design is that it was not possible to determine the gap size underneath the membrane. The silicon bulk etch time was kept to a minimum to barely release the structure, but there could be silicon peaks beneath the beams of the membrane. These peaks could possibly restrict motion of the membrane. It would be advantageous to use lateral electrostatic gaps, which can be more precisely defined in the layout. This is one of the primary motivations for a new sensor design.

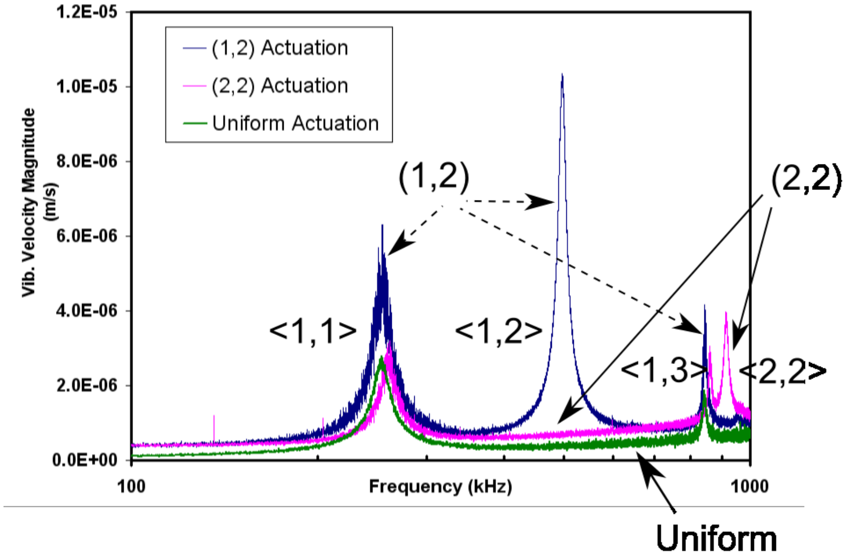

Figure 28: Frequency Responses for the different electrode actuation schemes: Uniform, (1,2), (2,2). The corresponding mode for each resonant peak is denoted with angle brackets, $\langle\rangle$.

The next prospective design for a gravimetric biosensor spawns from current work done in micromechanical filters. It is a combination of two ideas: (a) a glass disk operating in wine-glass bulk mode resonance [49] and (b) internal electrostatic transduction [50]. Figure 29 shows a diagram of the new sensor concept. The bulk material of the sensor will be silicon dioxide (glass). with aluminum on the perimeter for the actuation electrodes. There is aluminum on the perimeter where a DC bias voltage, Vdc, is applied. The AC actuation voltage signals is applied at the $Vin+$ and $Vin-$ electrodes, such that the two signals are 180 degrees out-of-phase. The bulk mode displacement is sensed via the capacitance changes at the $iout+$ and $iout-$ electrodes. The gaps between the electrodes will be filled with polystyrene polymer so that the top surface will be completely sealed, forming a boundary between the liquid and electronics. Figure 30 shows a cross-section of the disk resonator, as indicated by A-A' on Figure 29(a).

Some features of this design to be considered:

- The main advantage of this design is that the resonator will be oscillating in shear mode relative to the liquid so there will be less damping.
- The gap between the electrodes is a lateral dimension and can be controlled with the layout design. Across multiple devices, this gap length will be more consistent than with the membrane device.

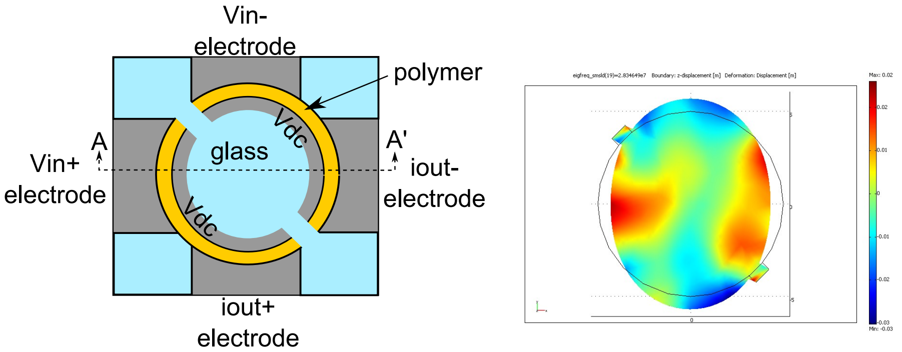

(a) Glass disk resonator with polystyrene polymer gap.
(b) Wine-glass bulk resonance mode.

Figure 29: New gravimetric biosensor concept design.

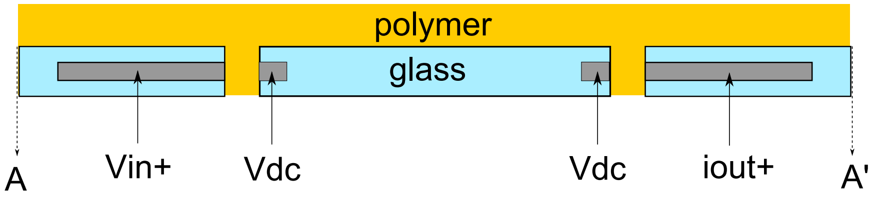

Figure 30: Disk resonator cross-section at A-A' on Figure 29(a). Drawing not to scale.

- The glass surface can be directly functionalized [51], circumventing the need to deposit polymer on the surface. Since it is difficult to add the same amount of polymer to each device, this will eliminate uncertainty of the mass addition due to polymer to the device.

- Since polystyrene has a higher dielectric constant (approx. 2.5) than air, this will result in greater electrostatic force for a given applied voltage. Other material with higher dielectric constants can also be investigated.

- Fully differential electrode configuration at the input and output [52] provides a closed current loop at the input and output. This should decrease the current loss through the anchor impedance. Figure 31 shows the equivalent circuit representation of the disk resonator, with V_{in} as the input voltage signals, i_{out} as the output current signals, i_{ft} as the feedthrough current, and i_x as the motional currents. This schematic incorporates the Butterworth-Van Dyke equivalent circuit of a resonator [30, 53]. The resonator is represented by a resistor, capacitor, and inductor in series, and the static capacitance of the electrodes is the parallel capacitance. Both i_x and i_{ft} are nulled at the proof mass node creating a virtual ground. No charge passes through the anchors and suspension enabling electrical energy to be stored in the resonator.

- Keeping the suspension anchors to a minimum of two will decrease the anchor

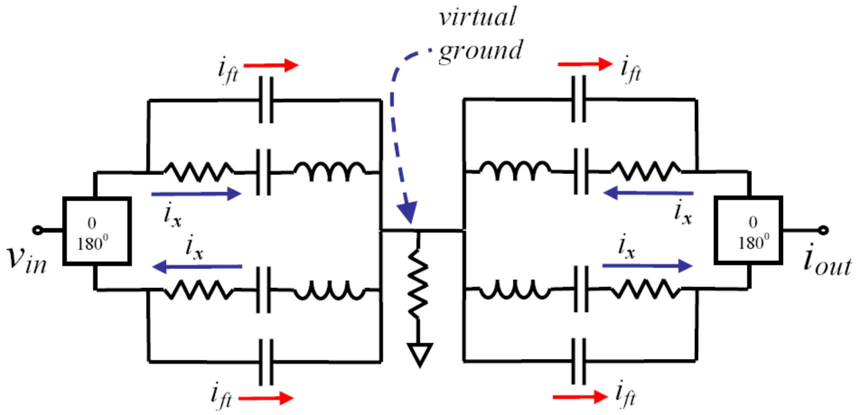

Figure 31: Fully differential electrode configuration [52].

loss, which will increase the Q-factor [49]. The reason for not using one anchor is because it is likely that there will be curl in the structure, so two anchors will keep the disk in plane during the release procedure.

- Using a different material for the anchors so that there is an acoustic impedance mismatch would decrease the acoustic loss from the resonator to the anchors [54]. It will be investigated which materials can be incorporated in the device fabrication process flow.
- An alternative to filling the gaps with polymer is to keep the air gaps but have a hydrophobic polymer coating on the solid parts around the gaps. It will be investigated whether it is possible to keep the liquid from passing through the gaps this way. There will be significant Q-factor loss due to the polymer, so this may be a solution to keep the air gap but still have a separation between the liquid and electronics.

7 Conclusion

A prototype of a CMOS MEMS membrane gravimetric biosensor has been fabricated and tested. The frequency response and corresponding modes has been obtained optically. The next step is to obtain the same frequency response electrically from the piezoresistors. The main issue with the membrane device is that out-of-plane displacement will probably be greatly damped by the liquid. Finite element analyses of acoustic fluid-structure interactions need to be completed to demonstrate whether the higher modes of the membrane will improve device performance in liquid. A new design of a gravimetric sensor operating in shear displacement relative to the liquid is another possibility for an improved gravimetric sensor in liquid.

References

[1] W. Ehrfeld and U. Ehrfeld, “Progress and profit through microtechnologies, Commercial applications of MEMS/MOEMS,” in *SPIE: Micromachining and Microfabrication Process Technology*, vol. 4557, pp. 1–10, 2001.

[2] A. Grayson, R. Shawgo, A. Johnson, N. Flynn, Y. Li, M. Cima, and R. Langer, “A BioMEMS review: MEMS technology for physiologically integrated devices,” in *Proceedings of IEEE*, vol. 92, pp. 6–21, 2004.

[3] R. A. Yotter, L. A. Lee, and D. M. Wilson, “Sensor technologies for monitoring metabolic activity in single cells-part I: optical methods,” *IEEE Sensors Journal*, vol. 4, pp. 395–411, August 2004.

[4] E. Thrush, O. Levi, K. Wang, J. S. H. Jr., and S. J. Smith, “Integrated semiconductor fluorescent detection system for biochip and biomedical applications,” in *2nd Annual International IEEE-EMBS Special Topic Conference on Microtechnologies in Medicine & Biology*, pp. 374–379, 2002.

[5] C.-H. Lin, S.-K. Hsiung, and G.-B. Lee, “High-throughput micro capillary electrophoresis chip for bio-analytical application utilizing multi-wavelength detection,” in *17th IEEE International Conference on Micro Electro Mechanical Systems (MEMS) 2004.*, pp. 304–307, 2004.

[6] H.-C. Yeh, E. Simone, C. Zhang, and T.-H. Wang, “Single bio-molecule detection with quantum dots in a microchannel,” in *17th IEEE International Conference on Micro Electro Mechanical Systems (MEMS)*, pp. 371–374, 2004.

[7] R. A. Yotter and D. M. Wilson, “Sensor technologies for monitoring metabolic activity in single cells-part II: nonoptical methods and applications,” *IEEE Sensors Journal*, vol. 4, pp. 412–429, August 2004.

[8] H. Suzuki, Y. Kato-Yamada, H. Noji, and S. Takeuchi, “Planar lipid membrane array for membrane protein chip,” in *17th IEEE International Conference on Micro Electro Mechanical Systems (MEMS)*, pp. 272–275, 2004.

[9] K.-S. Teh and L. Lin, “A polypyrrole-carbon-nanotube (PPy-MWNT) nanocomposite glucose sensor,” in *17th IEEE International Conference on Micro Electro Mechanical Systems (MEMS)*, pp. 395–398, 2004.

[10] M. Rouhanizadeh, T. Tang, C. Li, G. Soundararajan, C. Zhou, and T. Hsiai, “Applying indium oxide nanowires as sensitive and selective redox protein sensors,” in *17th IEEE International Conference on Micro Electro Mechanical Systems (MEMS)*, pp. 434–437, 2004.

[11] M. Cole, G. Sehra, J. Gardner, and V. Varadan, “Development of smart tongue devices for measurement of liquid properties,” *IEEE Sensors Journal*, vol. 4, pp. 543–550, October 2004.

[12] H. Zhang, M. S. Marma, E. S. Kim, C. E. McKenna, and M. E. Thompson, “Implantable resonant mass sensor for liquid biochemical sensing,” in *17th IEEE International Conference on Micro Electro Mechanical Systems (MEMS)*, pp. 347–350, 2004.

[13] M. Lei, A. Baldi, T. Pan, Y. Gu, R. A. Siegel, and B. Ziaie, “A hydrogel-based wireless chemical sensor,” in *17th IEEE International Conference on Micro Electro Mechanical Systems (MEMS) 2004.*, Micro Electro Mechanical Systems, pp. 391–394, IEEE, 2004.

[14] J. Chung, K.-H. Lee, and J. Lee, “Microfabricated glucose sensor based on single-walled carbon nanotubes,” in *17th IEEE International Conference on Micro Electro Mechanical Systems*, pp. 617–620, 2004.

[15] R. Rinaldi, P. Pompa, G. Maruccio, A. Biasco, P. Visconti, D. Pisignano, L. Blasi, N. Sgarbi, B. Krebs, and R. Cingolani, "Self-assembling of proteins and enzymes at nanoscale for biodevice applications," in *IEE Proceedings-Nanobiotechnology*, vol. 151, pp. 101–108, June 2004.

[16] A. Campifelli, C. Bartic, J.-M. Friedt, K. D. Keersmaecker, W. Laureyn, L. Francis, F. Frederix, G. Reekmans, A. Angelova, J. Suls, K. Bonroy, R. D. Palma, Z. Cheng, and G. Borghs, "Development of microelectronic based biosensors," in *Proceedings of the IEEE 2003 Custom Integrated Circuits Conference*, pp. 505–512, September 2003.

[17] K. Imano, R. Shimazaki, and S. Momozawa, "Measurement of Viscosity of Liquid Using Piezoceramic Disk Transducer with a Radial Expansion Mode," in *IEICE Trans. Fundamentals*, vol. E53-A, Jan. 2000.

[18] N. Wakatsuki and M. Bannai, "Study of LiTaO/sub 3/ shear wave resonator for viscosity sensor of polymer liquid in MHz range," in *IEEE Ultrasonics Symposium*, vol. 2, pp. 1334–1337, Oct. 2003.

[19] R. Crane and G. Fischer, "Analysis of a quartz crystal microbalance with coatings of finite viscosity," *J. Phys. D: Appl. Phys.*, vol. 12, pp. 2019–2026, Dec. 1979.

[20] R. White, "Acoustic sensors for physical, chemical and biochemical applications," in *Proceedings of the 1998 IEEE International Frequency Control Symposium*, pp. 587–594, 1998.

[21] A. Janshoff, H.-J. Galla, and C. Steinem, "Piezoelectric mass-sensing devices as biosensors - an alternative to optical biosensors?," *Angewandte Chemie Int. Ed.*, vol. 39, no. 22, pp. 4004–4032, 2000.

[22] N. V. Lavrik, M. J. Sepaniak, and P. G. Datskos, "Cantilever transducers as a platform for chemical and biological sensors," *Review of Scientific Instruments*, vol. 75, pp. 2229–2253, July 2004.

[23] J. Fritz, M. K. Baller, H. P. Lang, H. Rothuizen, P. Vettiger, E. Meyer, H. J. Gntherodt, C. Gerber, and J. K. G. 1, "Translating biomolecular recognition into nanomechanics," *Science*, vol. 288, pp. 316–318, April 2000.

[24] H. Zhang, M. S. Marma, E. S. Kim, C. E. McKenna, and M. E. Thompson, "A film bulk acoustic resonator in liquid environments," *J. Micromech. Microeng.*, vol. 15, pp. 1911–1916, Aug. 2005.

[25] J. Neumann and K. Gabriel, "A Fully-integrated CMOS-MEMS Audio Microphone," in *Transducers*, pp. 230–233, June 2003.

[26] D. Greve and J. Neumann, "Robust Capacitive MEMS Ultrasonics Transducers for Liquid Immersion," in *IEEE Ultrasonics Symposium*, pp. 581–584, 2003.

[27] A. Buhrdorf, A. Lohfink, S. Junge, P. Eccardt, and W. Benecke, "Fabrication and characterization of a new capacitive micromachined ultrasonic transducer (cmut) using polysilicon as membrane and sacrificial layer material," in *IEEE Symposium on Ultrasonics*, vol. 2, pp. 1951 – 1954, 2003.

[28] P. Eccardt, K. Niederer, and B. Fischer, "Micromachined transducers for ultrasound applications," in *IEEE Ultrasonics Symposium*, pp. 1609–1618, 1997.

[29] A. Bashford, D. Schindel, and D. Hutchins, "Micromachined ultrasonic capacitance transducers for immersion applications," *IEEE Transactions on Ultrasonics, Ferroelectrics and Frequency Control*, vol. 45, no. 2, pp. 367 – 375, 1998.

[30] H. Zhang and E. Kim, "Micromachined acoustic resonant mass sensor," *Journal of Microelectromechanical Systems (MEMS)*, vol. 14, pp. 699–706, August 2005.

[31] S. Bedair, "CMOS MEMS Oscillator for Gas Chemical Detection," Master's thesis, Carnegie Mellon University, December 2004.

[32] W. Zhang, R. Baskaran, and K. L. Turner, "Effect of cubic nonlinearity on autoparametrically amplified resonant MEMS mass sensor," *Sensors and Actuators A: Physical*, vol. 102, pp. 139–150, Dec. 2002.

[33] M. J. Bartkovsky, "Development of a MEMS based Membrane Gravimetric Biosensor." PhD Proposal, January 2004.

[34] W. Bowers, R. Chuan, and T. Duong, "A 200 MHz surface acoustic wave resonator mass microbalance," *Review of Scientific Instruments*, vol. 62, pp. 1624–1629, June 1991.

[35] "Commercial gravimetric quartz crystal microbalance system." website. http://www.q-sense.com.

[36] A. Clark, L. Whitehead, C. Haynes, and A. Kotlicki, "Novel resonant-frequency sensor to detect the kinetics of protein adsorption," *Review of Scientific Instruments*, vol. 73, pp. 4339–4346, December 2002.

[37] D. Pierce, Y. Kim, and J. Vig, "A temperature insensitive quartz microbalance," *IEEE Trans. UFFC*, vol. 45, pp. 1238–1245, Sept. 1998.

[38] M. Bartkovsky, A. Liao, G. Fedder, T. Przybycien, and S. Hauan, "The effect of a distributed mass loading on the frequency response of a mems mesh resonator," in *EMBC*, 2006. To be presented.

[39] B. Kloeck, *Sensors: A Comprehensive Survey. Vol. 7: Mechanical Sensors*, vol. 7, ch. 5: Piezoresistive Sensors, pp. 146–172. VCH, 1994.

[40] W. Young, *Roark's Formulas for Stress and Strain*. McGraw-Hill, 1989.

[41] S. A. Brooks, N. Dontha, C. B. Davis, J. K. Stuart, G. O'Neill, and W. G. Kuhr, "Segregation of micrometer-dimension biosensor elements on a variety of substrate surfaces," *Anal. Chem.*, vol. 72, pp. 3253–3259, 2000.

[42] M. Hengsakul and A. Cass, "Protein patterning with a photoactivatable derivative of biotin," *Bioconjugate Chemistry*, vol. 7, no. 2, pp. 249–254, 1996.

[43] D. Lyebyedyev and H.-C. Scheer, "Mask definition by nanoimprint lithography," in *Proc. SPIE*, vol. 4349, 2001.

[44] R. D. Deegan, "Pattern formation in drying drops," *Physical Review E*, vol. 61, pp. 475–485, January 2000.

[45] J. Valentine, T. Przybycien, and S. Hauan, "Modeling and design of a mems-based biosensor," in *AIChe Annual Meeting*, no. 197h, Nov. 2003.

[46] J. E. Valentine, "Optimal design of acoustic wave biochemical sensors using mems (phd proposal)," tech. rep., Carnegie Mellon University, 2005.

[47] "Jazz semiconductor," 2006. [Online; accessed 16-January-2006].

[48] "Universal laser systems, inc.." http://www.ulsinc.com. Manufacturer of portable laser systems.

[49] M. Abdelmoneum, M. Demirci, and C.-C. Nguyen, "Stemless wine-glass-mode disk micromechanical resonators," in *IEEE Int'l Conf. MEMS*, pp. 698–701, 2003.

[50] S. A. Bhave and R. T. Howe, “Internal Electrostatic Transduction for Bulk-Mode MEMS Resonators,” in *Solid-State Sensor, Actuator and Microsystems Workshop*, pp. 59–60, June 2004.

[51] G. A. Campbell and R. Matharasan, “Detection of pathogen Escherichia coli O157:H7 using self-excited PZT-glass microcantilevers,” *Biosensors and Bioelectronics*, vol. 21, pp. 462–473, 2005.

[52] S. A. Bhave, D. Gao, R. Maboudian, and R. T. Howe, “Fully-Differential Poly-SiC Lame-Mode Resonator and Checkerboard Filter,” in *18th IEEE International Conference on Micro Electro Mechanical Systems (MEMS)*, pp. 223–226, 2005.

[53] S. J. Martin, V. E. Granstaff, and G. C. Frye, “Characterization of a quartz crystal microbalance with simultaneous mass and liquid loading,” *Analytical Chemistry*, vol. 63, pp. 805–808, October 1991.

[54] J. Wang, J. Butler, T. Feygelson, and C.-C. Nguyen, “1.51-GHz Nanocrystalline Diamond Micromechanical Disk Resonator With Material-Mismatched Isolating Support,” in *17th Int. IEEE Micro Electro Mechanical Systems (MEMS) Conf.*, pp. 641–644, 2004.